

Average Ionospheric Electric Field Morphologies during Geomagnetic Storm Phases

M.-T. Walach¹, A. Grocott¹, S. E. Milan²

¹Lancaster University, Lancaster, LA1 4YW, UK

²University of Leicester, Leicester, LE1 7RH, UK

Key Points:

- Using Principal Component Analysis on SuperDARN data we identify the primary contributing basis convection patterns to ionospheric electric field morphologies during geomagnetic storm times
- The first 6 eigenvectors of the analysis provide over 90% of the total variance
- The main changes in the electric field that are ordered by storm phase are an enhancement of the convection potential and a rotation of the dayside convection throat

Corresponding author: Maria-Theresia Walach, m.walach@lancaster.ac.uk

14 **Abstract**

15 We utilise Principal Component Analysis to identify and quantify the primary electric
16 potential morphologies during geomagnetic storms. Ordering data from the Super Dual
17 Auroral Radar Network (SuperDARN) by geomagnetic storm phase, we are able to dis-
18 cern changes that occur in association with the development of the storm phases. We
19 find that the first 6 eigenvectors provide over $\sim 90\%$ of the variability, providing us with
20 a robust analysis tool to quantify the main changes in the morphologies. Studying the
21 first 6 eigenvectors and their eigenvalues with respect to storm phase shows that the pri-
22 mary changes in the morphologies with respect to storm phase are the convection po-
23 tential enhancing and the dayside throat rotating from pointing towards the early af-
24 ternoon sector to being more sunward aligned during the main phase of the storm. We
25 find that the ionospheric electric potential increases through the main phase and then
26 decreases after the end of the main phase is reached. The dayside convection throat points
27 towards the afternoon sector before the main phase and then as the potential increases
28 throughout the main phase, the dayside throat rotates towards magnetic noon. Further-
29 more, we find that a two cell convection pattern is dominant throughout and that the
30 dusk cell is overall stronger than the dawn cell.

31 **Plain Language Summary**

32 During geomagnetic storms we see extreme changes to Earth's magnetic field struc-
33 ture. This is mainly due to an enhancement of electrical currents in geospace. This changes
34 the Earth's magnetic environment, due to which we also see changes in the ionosphere,
35 the layer of charged particles making up the top of the atmosphere where the current
36 systems close. A geomagnetic storm has three phases: the initial phase, which is a pre-
37 cursor to the storm, the main phase where the current systems enhance abruptly, and
38 a recovery phase. In this paper we use a technique commonly used for pattern recogni-
39 tion on radar data to work out the changes to the average ionospheric flows. We find that
40 most of the changes happen on the dayside. This means the average storm dynamics are
41 driven directly by the solar wind.

42 **1 Introduction**

43 Geomagnetic storms are understood to be enhancements in the Earth's ring cur-
44 rent (Akasofu & Chapman, 1961; Gonzalez et al., 1994). This westward-flowing current

45 causes large-scale deviations in the Earth's magnetic field, such that they can be measured
46 on the ground (e.g. Graham, 1724; Chapman & Dyson, 1918; Chapman & Ferraro, 1930;
47 Chapman & Bartels, 1940; Singer, 1957; Daglis et al., 1999). At mid-latitudes, this ef-
48 fect is strongest and registers as a southward deviation in the horizontal north-south mag-
49 netometer measurements. These measurements are often combined to give a magnetic
50 index, which can be used to identify storms, such as the Dst index (Sugiura, 1964) or
51 Sym-H index (Iyemori, 1990).

52 Notable effects of geomagnetic storms not only include changes in the global mag-
53 netic field and strengthening of the magnetospheric and ionospheric current systems, but
54 also changes in the ionosphere, such as higher measured densities in the total electron
55 content in the mid-to-low latitudes, which can drift and enhance ionospheric densities
56 at higher latitudes to form storm-enhanced densities (SEDs) and thus also enter the po-
57 lar cap, forming tongues-of-ionization (TOIs) (e.g. Foster, 1993; Huba et al., 2005; Lin
58 et al., 2005; Mannucci et al., 2008; Thomas et al., 2013; Zou et al., 2013, 2014, and ref-
59 erences therein). SEDs in particular have been linked to equatorward expansion of the
60 convection pattern (Zou et al., 2013, 2014) and it is thus important to understand the
61 high-latitude ionospheric electric field as it evolves throughout geomagnetic storms as
62 it will help us understand plasma transport in the ionosphere and magnetosphere.

63 Whilst ground magnetometer studies can be used to infer the ionospheric electric
64 field (Kamide et al., 1981), direct measurements of plasma convection can also be utilised
65 to build maps of the high-to-mid latitude ionospheric electric fields (e.g. Hairston & Heelis,
66 1993; Ruohoniemi & Greenwald, 1996). In a previous study, Walach and Grocott (2019)
67 (from here on referred to as WG19) studied ionospheric measurements from the Super
68 Dual Auroral Radar Network (SuperDARN) during the three phases of geomagnetic storms:
69 the initial, main and recovery phase, identified using Sym-H.

70 WG19 examined the general trends in the SuperDARN data during geomagnetic
71 storms, such as latitudinal expansion of the ionospheric convection maps, data coverage,
72 data availability, cross polar cap potential (i.e. convection strength), in relation to so-
73 lar wind and geomagnetic conditions. The study also compared statistically the responses
74 of these measured parameters during geomagnetic storm phases, to periods of disturbed
75 geomagnetic activity, irrespective of storm phase, as well as high solar wind driving when
76 no storms occurred. One of the primary results of this paper was that the storm phases,

77 as well as the ionospheric responses measured by SuperDARN are closely tied to the so-
78 lar wind driving of the system, which matches previous results (e.g. Loewe & Prölss, 1997;
79 Gillies et al., 2011): During the main phase of a geomagnetic storm, higher solar wind
80 driving due to southward interplanetary magnetic field (negative B_Z) enhances the cur-
81 rent systems connecting the ionosphere with the magnetosphere. We thus see a higher
82 cross polar cap potential, as well as an enhanced Sym-H index, matching our understand-
83 ing of how the system works (e.g. Milan et al., 2017). WG19 showed that throughout
84 a geomagnetic storm there is some asymmetry in the two-cell convection pattern mea-
85 sured by SuperDARN, with the dusk cell being much stronger than the dawn cell, as well
86 as changes throughout the storms in the location where the fastest flows are measured
87 in the ionosphere: This is primarily on the dayside, though in the initial and recovery
88 phase the fastest flows are primarily measured in the noon to early morning sectors whereas
89 during the main phase of a storm, this is shifted towards the afternoon sectors. WG19
90 also found that the return flow boundary (the latitudinal location where antisunward
91 flows neighbour the sunward flows) and the Heppner-Maynard boundary (Heppner & May-
92 nard, 1987) (the boundary where the high-latitude ionospheric convection pattern ter-
93 minates) move throughout the storm phases, as does the latitudinal distance between
94 them.

95 Other previous studies using SuperDARN data from geomagnetic storm periods
96 have looked at the number of scatter echoes and line-of-sight velocities in relation to sud-
97 den storm commencements (SSC) and sudden commencements (SC) (e.g. Gillies et al.,
98 2012; Kane & Makarevich, 2010), but without a detailed quantitative analysis of iono-
99 spheric convection morphologies. A further statistical study by (Gabrielse et al., 2019)
100 compared the mesoscale flows measured by SuperDARN during the main phases and re-
101 covery phases, as well as coronal mass ejection (CME) and highspeed stream (HSS) storms.
102 Whilst WG19 did not split the data into the exact same categories, the results broadly
103 agree with these previous studies. Here we only focus on the geomagnetic storm phases
104 to learn about the average ionospheric behaviour. Whilst WG19 answers some basic ques-
105 tions on the morphology and latitudinal extent of ionospheric convection during the phases
106 of a geomagnetic storm, we will examine the morphologies of geomagnetic storms in more
107 detail here. In this paper, we will study these data further to answer the following ques-
108 tion: How do ionospheric convection morphologies change throughout the storm phases?

109 We answer this question by utilising an objective method for dimensionality reduc-
110 tion (Principal Component Analysis (e.g. Joliffe, 2002)), which will tell us what the pri-
111 mary morphologies in the data are with respect to storm phase.

112 **2 Data**

113 There are two primary datasets used in this study: The geomagnetic storm list and
114 the SuperDARN data, which we describe in this section.

115 **2.1 Geomagnetic Storms**

116 The geomagnetic storm list is published by WG19 and can be found in their sup-
117plementary material. It is formed by applying an automatic identification algorithm to
118 the Sym-H index, which reflects enhancements in the global ring current (Iyemori, 1990).
119 The algorithm identifies the initial, main and recovery phases of geomagnetic storms, sim-
120ilar to Hutchinson et al. (2011), which allows us to draw conclusions about the phenom-
121ena associated with the progression of storms. In brief, the initial phase of a geomag-
122netic storm is classified by a positive excursion in the Sym-H index, associated with an
123increase in the Ferraro-Chapman currents along the magnetopause, followed by a decrease
124to below -80 nT during the main phase, where the ring current enhances. The minimum
125in Sym-H coincides with the end of the main phase, which is followed by a gradual in-
126crease to normal values, known as the recovery phase. For further detail, the reader is
127referred to WG19.

128 **2.2 SuperDARN**

129 SuperDARN consists of high-frequency coherent scatter radars built to study iono-
130spheric convection by means of Doppler-shifted, pulse sequences (e.g. Greenwald et al.,
1311995; Ruohoniemi & Greenwald, 1996; Chisham et al., 2007; Nishitani et al., 2019). Mea-
132surements by this large-scale network of radars are used to construct a high-time res-
133olution picture of high-latitude ionospheric convection (Ruohoniemi & Baker, 1998).

134 With the expansion of the SuperDARN network to mid-latitudes, we are able to
135study the dynamics of the high-to-mid-latitude ionospheric convection with unprecedented
136coverage (Nishitani et al., 2019). One of the findings by WG19 was that the high-latitude
137convection maps which can be produced with SuperDARN data can expand to 40° of

138 geomagnetic latitude during disturbed times, which was not accounted for in previous
 139 versions of the SuperDARN Radar Software Toolkit (RST versions < 4.2), which had
 140 a cut-off of 50° magnetic latitude. The finding of this expansion matches magnetome-
 141 ter and spacecraft measurements from previous studies (e.g. Wilson et al., 2001; Kikuchi
 142 et al., 2008).

143 The SuperDARN data used here were therefore processed using the Radar Soft-
 144 ware Toolkit (RST) (SuperDARN Data Analysis Working Group et al., 2018), which is
 145 specifically designed to accomodate SuperDARN observations down to 40° of magnetic
 146 latitude. Typically, to make SuperDARN convection maps several steps of processing have
 147 to be followed: 1) Using RST, an autocorrelation function is fitted to the raw radar data.
 148 This produces fitacf files, which store the line-of-sight velocity data. 2) The data is then
 149 gridded onto an equal area latitude-longitude grid (see equation 1 from Ruohoniemi &
 150 Baker, 1998) and split into two minute cadence records. 3) Data from different radars
 151 are combined and the spherical harmonic fitting algorithm is performed which fits an elec-
 152 trostatic potential in terms of spherical harmonic functions to the data (Ruohoniemi &
 153 Greenwald, 1996; Ruohoniemi & Baker, 1998). When this fitting is performed, typically
 154 a background model, parameterised by solar wind conditions is used, to infill informa-
 155 tion in the case of data gaps (e.g. Thomas & Shepherd, 2018). Alongside this, a Heppner-
 156 Maynard boundary (HMB) (Heppner & Maynard, 1987), the low-latitude boundary of
 157 the convection pattern where the flows approach zero, can either be specified or be cho-
 158 sen using the data. This is to constrain the convection pattern when the spherical har-
 159 monic fit is applied (Shepherd & Ruohoniemi, 2000). For typical 2-minute convection
 160 maps, it is appropriate to use the data to find a threshold of three radar velocity mea-
 161 surements of greater than 100 ms^{-1} for the HMB (Imber et al., 2013).

162 For the purpose of this study, we make 2 minute cadence superposed epoch con-
 163 vection maps, where data from the different storms are combined. This differs slightly
 164 to the usual steps outlined above and is explained further in the following section.

165 We utilise the same storm list and the same gridded SuperDARN data, spanning
 166 from 2010-2016, as published in WG19. We have 54 storms with the median storm du-
 167 ration for each storm phase of 9.8 hours for the initial phase, 4.5 hours for the main phase
 168 and 27.9 hours for the recovery phase.

3 Method

In order to study the characteristic ionospheric convection morphologies of the storms in detail, we make a superposed epoch analysis. Similarly to Hutchinson et al. (2011) and Wharton et al. (2020), we make a superposed epoch analysis of the storms which treats each storm phase independently and scales each phase to the beginning and end, using the median duration. This means that each storm phase duration is scaled to be the same and we can thus compare average characteristics across storms.

We apply our method to the SuperDARN data to make average storm convection maps, which are parameterised by storm phase and median duration: We use the gridded data from the previous study (WG19), and write new convection maps for each storm phase, which are thus time-normalised and comprise the data from all storms. In order to make the convection maps, we write files with all the data and run the map-fitting procedure using RST v4.2 (SuperDARN Data Analysis Working Group et al., 2018) and a 6th order spherical harmonic expansion (Ruohoniemi & Greenwald, 1996). This differs slightly to the usual method described earlier: In order to make the storm maps, no statistical background model was used, as the data coverage is very good when combining data from 7 years of geomagnetic storms. As data coverage at lower latitudes can be sparse, especially during the initial phase, the automatic HMB algorithm can select unrealistic boundaries. We avoid this by forcing the HMB to match the lower quartile of the distribution of HMBs from the individual maps per timestep per phase (this is shown in Fig. 8 in WG19). Examples of these average convection maps are given in Figure 1, which shows a map from the beginning of each storm phase. All other maps are included in the form of animations as supplementary material or can be downloaded as convection map files from Lancaster University’s research archive (PURE) (Walach, 2020).

From Fig. 1 we see that the convection patterns are different at the beginning of each storm phase: As expected, at the beginning of the initial phase the convection pattern is relatively small and the ionospheric convection velocities are low, whereas at the beginning of the main phase, the familiar two-cell convection pattern (e.g. Ruohoniemi & Greenwald, 1996) is enhanced and expanded, with fast return flows seen on the dusk-side. From examining these convection maps (see also supplementary material), we see that the two-cell pattern stays strong and expanded throughout the main phase. Fig. 1 and the supplementary material shows that this is further enhanced at the beginning

201 of the recovery phase. We see from the supplementary information that the fast flows,
 202 strong convection and expanded pattern stays prevalent long into the recovery phase,
 203 but start to decrease after the main phase ends.

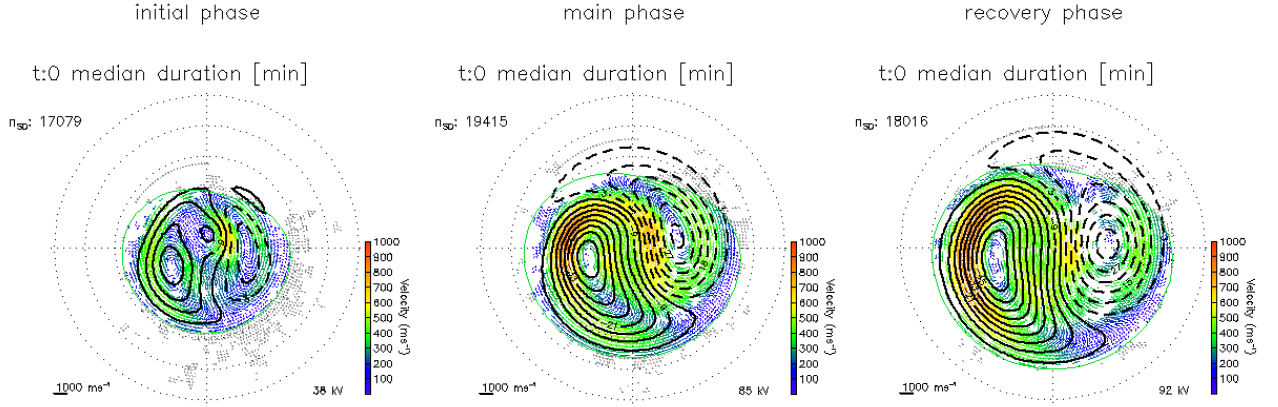


Figure 1. Example SuperDARN convection maps from the Superposed Epoch Analysis showing the first map of the initial (left), main (centre) and recovery phase (right), respectively. Each panel shows a map in the geomagnetic (AACGM) coordinates, whereby noon is towards the top of the page and dusk is towards the left and the grey concentric circles show equal magnetic latitudes of 10° , ranging from $80-40^\circ$. The ionospheric flow vectors are colour coded by magnitude, and the electrostatic potentials are shown as equipotentials at 3 kV steps (in black). The green boundary in each panel indicates the Heppner-Maynard boundary.

204 Studying these average maps is useful to observe obvious changes in the convec-
 205 tion, such as deviations from the two-cell convection regime, expansions and contractions,
 206 or patches of fast flows. In order to quantify changes in the convection morphologies fur-
 207 ther we now utilise principal component analysis on the data. This is a well-known tech-
 208 nique for pattern recognition and is also known under different names, such as empir-
 209 ical orthogonal functions, and has been used successfully for geophysical datasets (see
 210 Baker et al., 2003; Cousins et al., 2013, 2015; Milan et al., 2015; Shore et al., 2018; Shi
 211 et al., 2020; Kim et al., 2012, and references therein). An alternative method is to use
 212 the spherical harmonics to examine changes (e.g. Grocott et al., 2012), but in this case
 213 the components are predetermined, which limits their interpretability. In PCA the com-
 214 ponents are defined by the data which allows us to find the main constituents which make

215 up the patterns. Overall, this allows us to quantify the main components to the patterns
 216 and see how they change over time.

217 The underlying principle is that the dataset can be decomposed into a series of ba-
 218 sis functions which reveal underlying correlations within the data. In our case, the dataset
 219 is made of the electrostatic potential maps, Φ_t (where $t=0,\dots,m$), such that $m = 1266$
 220 (the median storm duration at a time resolution of 2 minutes) and each Φ_t has n -elements,
 221 where n is given by the number of latitude by longitude grid points (2° resolution). All
 222 the observations can be expressed as one $m \times n$ matrix (Φ). The covariance matrix Σ
 223 is then given by $\Sigma = \frac{1}{m} \Phi^T \Phi$, where Φ^T is the transpose of Φ . The data Φ_t can be ex-
 224 pressed (or reconstructed) in terms of eigenvectors, \mathbf{X}_i , of the covariance matrix Σ and
 225 their components, α_i , such that

$$226 \quad \Phi_t = \sum_{i=1}^n \alpha_i \mathbf{X}_i. \quad (1)$$

227 This means components at a given time, α_i , are given by

$$228 \quad \alpha_i = \Phi_t \cdot \mathbf{X}_i. \quad (2)$$

229 Applying this method to the convection maps allows us to quantify and detect mor-
 230 phological changes automatically, as well as determine the primary components which
 231 make up the ionospheric electric field. In order to do this, we first scale all the ionospheric
 232 convection maps, such that they are the same size. This is necessary for the principal
 233 component analysis to work. Using different pattern sizes would involve padding areas
 234 with no data with zeros and result with no correlation between the majority of gridpoints
 235 and thus the principal component analysis method would not work. Whilst changing the
 236 size of the pattern will make the expansions and contractions invisible for the Principal
 237 Component Analysis, this information is kept, so it can be studied in conjunction with
 238 the components later. We discuss this again later in the paper and also address the ex-
 239 pansions and contractions in WG19. We resize the maps by scaling by the Heppner-Maynard
 240 boundary (Heppner & Maynard, 1987) at midnight to 50° of magnetic co-latitude. We
 241 then take the electrostatic potential from each map using a 2° latitude by 2° longitude
 242 resolution. This allows us to make each map into a 1-dimensional 4500 line matrix ($n =$
 243 4500). We then calculate the mean of all the maps and subtract this from each individ-
 244 ual map. On the remaining dataset we perform the eigen decomposition using the House-
 245 holder method of eigen-decomposition (Press et al., 2007). Using only data from geo-
 246 magnetic storm times for the principle component analysis means that the only bias is

247 in our event selection, which was done using the automatic algorithm from WG19 on the
 248 Sym-H index. It is worth noting that whilst selecting by geomagnetic storm times only
 249 means we can analyse the storm-time morphologies specifically, we also impose a selec-
 250 tion bias: although we include some quieter times during the recovery phase of the storms,
 251 this selection bias results in our mean and eigenvector patterns looking different from
 252 analyses done in previous studies (e.g. Cousins et al. (2013) used an interval which had
 253 very little geomagnetic activity and Milan (2015) used all of the available AMPERE data)
 254 and we comment on this further in the discussion section.

255 4 Results

256 By examining the the eigenvalues, we can determine the importance of each of the
 257 eigenvectors (i.e. the component patterns that are added or subtracted together to make
 258 the convection maps). Figure 2 shows the cumulative explained variance, expressed in
 259 percentages. We see immediately that the curve converges fast: The orange dotted and
 260 dashed lines show $>80\%$ and $>95\%$ cut-off values, respectively. Whilst we have 4500 eigen-
 261 values and vectors, we see from Fig. 2 that we do not need all these values to express
 262 the majority of the variability in the electric potential patterns. In fact, the variance con-
 263 verges fast enough that the first 6 eigenvectors explain over 90% of the variance (this is
 264 shown by the green lines). In the following parts of the manuscript we will thus focus
 265 our attention on the first 6 eigenvectors and components and examine these further.

266 By adding or subtracting factors of \mathbf{X}_i (where $i=1,\dots,4500$) we are able to thus re-
 267 construct the initial maps. These factors as a function of time are given by the compo-
 268 nents, α_i . To simplify the interpretation of what proportion of the CPCP each compo-
 269 nent pattern holds, we have normalised each component pattern by a factor, f_i , such that
 270 terms in equation 2 become $\mathbf{X}_i^* = \mathbf{X}_i/f_i$ and the range of each \mathbf{X}_i^* is approximately
 271 equal to one. We also scale α_i , such that $\alpha_i^* = (\alpha_i \times f_i)$, which represents the approx-
 272 imate CPCP each component holds and we can thus analyse this with respect to time
 273 through the storm phase. We now examine these terms ($i = 0\dots6$) in more detail.

274 Figure 3 shows the primary electrostatic potential pattern components: the panel
 275 in the top left corner shows the mean pattern which was subtracted from all maps be-
 276 fore applying the principal component analysis. The other panels show a scaled version
 277 of the first 6 eigenvectors (i.e. the most dominant pattern components). The pattern com-

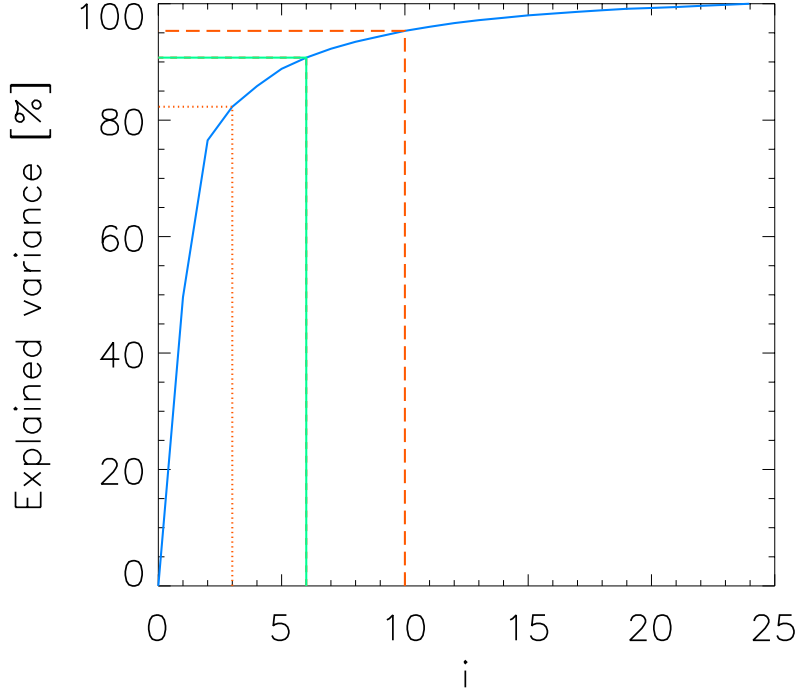


Figure 2. Explained variance (the first 25 eigenvalues) shown cumulatively in % of the total variance. The orange dotted and dashed lines show the 80%, and 95% cut-off values, respectively, whereas the green line shows the cut-off value of the first 6 eigenvalues ($\sim 90\%$).

278 ponents $\mathbf{X}_{1,\dots,6}^*$ are normalised by their CPCP, such that the colour scale approximately
 279 represent a range of 1. We will refer to this same normalisation factor, f_i , again later,
 280 as it will aid the interpretation of Figure 4. Each panel shows the eigenvector as a map
 281 in the same coordinate system as Fig. 1, whereby the magnetic pole is in the centre, noon
 282 is towards the top of the page, and dusk towards the left. The concentric dashed circles
 283 outline equal latitudes at 10° separation. As expected, the mean shows that a clear two-
 284 cell electric potential is dominant, with an enhancement in the dusk cell. What is less
 285 expected is that we also see an anti-clockwise rotation. We see that \mathbf{X}_1^* is able to pro-
 286 vide an increase or decrease in the two-cell convection potential with adding or subtract-
 287 ing the asymmetry from the mean pattern due to the similar rotation. \mathbf{X}_2^* provides mor-
 288 phological asymmetry by being an almost uniformly negative potential, so adding or
 289 subtracting this would strengthen one cell and weaken the other, or vice-versa. $\mathbf{X}_{3,\dots,6}^*$
 290 provide a rotation to the dayside convection throat. Overall, we see from $\mathbf{X}_{1,\dots,6}^*$ that
 291 the majority of the variability in the electric potential on the dayside will be larger than

292 on the nightside as the electrostatic potential values seen on the dayside portion are higher
 293 and the spatial gradients are more pronounced than on the nightside.

294 The top panel of Figure 4 shows a superposed epoch analysis of the interplanetary
 295 magnetic field components, B_{IMF} , resolved into the GSM (Geocentric Sola Magneto-
 296 spheric) coordinates with X in light green, Y in turquoise, and Z in dark blue. The sec-
 297 ond panel from the top shows the Heppner-Maynard boundary (in black) which the maps
 298 were scaled by, as well as the number of backscatter points per average SuperDARN map
 299 (in rose). This is followed by the median Sym-H and then the first six components, all
 300 as a function of storm phase-adjusted time, which are shown in grey. The black lines show
 301 the low pass filtered curve, using a 60-min centred kernel window to show the large scale
 302 changes more clearly. The first vertical dashed blue line marks the end of the initial phase
 303 and thus the beginning of the main phase and the second dashed blue line shows the end
 304 of the main phase and the beginning of the recovery phase.

305 We observe that the B_Z component is clearly enhanced, especially during the main
 306 phase of the storm and that the number of backscatter points per SuperDARN map is
 307 high (this can also be seen from the animations MS01-MS03 in the Supporting Informa-
 308 tion).

309 The components can be of positive or negative values. The magnitude of the val-
 310 ues indicate how much the normalised eigenvectors, \mathbf{X}_i^* , have to be amplified by and the
 311 positive or negative indicates whether or not this has to be added to or subtracted from
 312 the mean and the other components to compose the full pattern for this timestep (see
 313 also equations 1 and 2). The benefit of scaling α_i by f_i (i.e. the true range of \mathbf{X}_i), is that
 314 the scaled components α_i^* represent the CPCP of each pattern and thus aids interpre-
 315 tation.

316 We see immediately that much of the variability in the components is dominated
 317 by noise, but focusing on the black curves we see a few clear changes in α_i^* with respect
 318 to the geomagnetic storm phases: α_1^* shows a clear changes which mirrors the HMB and
 319 Sym-H closely. At the start of the main phase, this value decreases abruptly, then stays
 320 negative and then starts to increase gradually throughout the recovery phase. α_3^* is pri-
 321 marily negative throughout the initial phase, then increases to a positive value through
 322 the main phase and remains primarily positive throughout the recovery phase.

Table 1. t , $|r|$ and p values between Sym-H; B_Y ; B_Z and each component shown in Figure 4 (black smoothed lines).

i	Sym-H:			B_Y :			B_Z :		
	t [min]	$ r $	p	t [min]	$ r $	p	t [min]	$ r $	p
1	0	0.803	0.000	329	0.216	1.294×10^{-27}	15	0.815	0.000
2	166	0.593	0.000	119	0.307	0.000	239	0.502	0.000
3	49	0.409	0.000	26	0.189	2.348×10^{-21}	360	0.267	2.709×10^{-41}
4	260	0.335	0.000	7	0.428	0.000	141	0.371	0.000
5	75	0.469	0.000	22	0.412	0.000	196	0.404	0.000
6	128	0.521	0.000	61	0.370	0.000	148	0.518	0.000

323 To analyse these changes further with respect to IMF B_Y and B_Z and Sym-H, we
 324 perform a cross-correlation analysis between each of these parameters and the compo-
 325 nents. To highlight the variations over larger timescales, we use the smoothed compo-
 326 nents from Fig. 4. The best correlation coefficient, $|r|$, of each of these and their respec-
 327 tive lag times, t , are given in 1. We also show p for each correlation pair, which is de-
 328 fined as the significance of the correlation. This is defined by Press et al. (2007) as

$$329 \quad p = \operatorname{erfc} \left(\frac{|r|\sqrt{N}}{\sqrt{2}} \right), \quad (3)$$

330 where erfc is the complementary error function and N is the number of datapoints, which
 331 is, as defined earlier, m . This value expresses the probability that in the null hypoth-
 332 esis of two values being uncorrelated, $|r|$ should be larger than its observed value. A small
 333 value of p (i.e. $p = 0$) thus indicates that the correlation is significant.

334 Table 1 shows that p is generally low, and $p = 0$ for the cross-correlation between
 335 the first 6 components and Sym-H. This means these correlations are statistically sig-
 336 nificant. We see that the first component in particular is highly correlated with both Sym-
 337 H and B_Z , with a time lag, $t = 0$. This means that changes in this component are cor-
 338 related with changes in Sym-H (i.e. the storm phases) and B_Z (i.e. solar wind driving).
 339 As i increases, $|r|$ tends to decrease. The correlational pairs with B_Y are in general lower
 340 than the correlations with B_Z , which means the time variability we see in the compo-
 341 nents tend to correlate better with B_Z than B_Y . The notable exceptions here are α_4^* ,

342 and α_5^* , which are the only components where the correlations with B_Y are higher than
 343 the correlations with B_Z .

344 The time lags are more difficult to interpret but indicate several patterns: The ma-
 345 jority of the convection pattern (i.e. α_1^* , which holds more than 75% of the variance) shows
 346 its best correlation at $t = 0$, which means this component's contribution is mostly re-
 347 lated to Sym-H as this is how the storm phases are defined. The timelag is within the
 348 range $0 < t < 1$ hours for the pairs α_3^* to α_6^* and B_y , which indicates that these com-
 349 ponents may be driven by the IMF B_Y component. We further note, that for any pairs
 350 where $|r|$ is very low (< 0.3), t is high, which we interpret to not be meaningful and thus
 351 do not comment further on these.

352 5 Discussion

353 In Fig. 4 we show that the Heppner-Maynard boundary expands to $< 50^\circ$ magnetic
 354 latitude approaching the main phase and stays expanded, well into the recovery phase
 355 when considering the lower quartile of the distribution shown in WG19. It is possible
 356 that in reality, this expansion moves to lower latitudes than 40° for individual storms
 357 but our observations are limited by the geographical location of the SuperDARN radars
 358 and our choice of the HMB. This expansion is coincident with the IMF B_Z component
 359 becoming more southward, leading to a higher dayside reconnection rate and thus more
 360 rapid opening of magnetic flux (Siscoe & Huang, 1985; Cowley & Lockwood, 1992; Mi-
 361 lan et al., 2012; Walach et al., 2017). This means an expansion of the open-closed field
 362 line boundary occurs, which happens in tandem with the expansion of the convection
 363 pattern observed here (see also WG19). The high-latitude ionospheric electric field and
 364 thus convection pattern is an important mechanism for plasma transport and thus its
 365 expansion will mean the circulation of plasma at lower latitudes than was previously cir-
 366 culated by the high-latitude convection pattern. Zou et al. (2013) also showed that the
 367 convection pattern expanding during geomagnetic storms plays an important role in the
 368 generation and propagation of storm-enhanced densities (SEDs) seen on the dayside at
 369 mid-latitudes: Zou et al. (2013) found that there are two parts to SEDs, with the equa-
 370 torward expansion of the convection pattern being the primary driver for the SED for-
 371 mation.

372 We find that the first six eigenvalues hold $>90\%$ of the variability in ionospheric
 373 electric potential during storms (see Fig. 2). The first eigenvector (see \mathbf{X}_1^* in Fig. 3) rep-
 374 represents a dual-cell convection pattern, associated with the Dungey-cycle (e.g. Dungey,
 375 1961, 1963; Milan, 2015; Walach et al., 2017); when α_1^* is negative \mathbf{X}_1^* is subtracted from
 376 the mean, producing a more enhanced dual-cell convection pattern. We see from Fig.
 377 4 that this is the case throughout the main phase of the storm, as well as the majority
 378 of the recovery phase, peaking towards the end of the main phase, when solar wind driv-
 379 ing is highest. This matches the findings of WG19, which showed that this is also when
 380 the cross polar cap potential is highest. We see from Fig. 4 that the CPCP addition from
 381 the first component changes from ~ 20 kV in the initial phase to ~ -40 during the main
 382 phase, which is a step change of 60 kV and slightly higher than the 40 kV step change
 383 in CPCP that was seen in WG19. This highlights that whilst this component drives a
 384 lot of the storm phase change related variability, more components need to be added to
 385 get an accurate representation of the CPCP. We see from Fig. 4 that the following com-
 386 ponents contain slightly lower magnitudes of the potential, and decrease with each com-
 387 ponent.

388 The third, fourth, fifth and sixth components only add up to ~ 10 kV to the con-
 389 vection pattern at their peak, which is minimal in the context of a CPCP between 40
 390 to 80 kV. It is confirmed by table 1 that what looks like noise in Fig. 4 in some of the
 391 higher order components (α_4^* and α_5^*), is indeed very weakly correlated with Sym-H, which
 392 means these changes are not related to the storm phases. Whilst α_6^* shows a higher cor-
 393 relation ($|r|=0.521$), it adds however less to the total CPCP and is thus less impor-
 394 tant. We see that the correlation between α_1^* and Sym-H is on the other hand very high
 395 ($|r|=0.803$) and significant ($p=0.00$), which means this component is clearly correlated
 396 with the storm phases. This component is also highly correlated with B_Z , which is no
 397 surprise, given the high levels of solar wind driving seen during geomagnetic storms.

398 The second eigenvector (\mathbf{X}_2^* in Fig. 3) represents an almost uniform increase or de-
 399 crease in the potentials and the third eigenvector (\mathbf{X}_3^*) resembles the classic dual cell con-
 400 vection pattern but with a rotation towards dawn. The fourth to sixth eigenvectors (\mathbf{X}_4^*
 401 to \mathbf{X}_6^* in Fig. 3) represent asymmetric dawn-dusk changes to the patterns, which appear
 402 to mainly impact the pattern on the dayside, though can rotate the nightside convec-
 403 tion throat as well. It is notable that the main eigenvectors and components do not show
 404 clear morphological changes on the nightside in comparison to the dayside: Fig. 3 shows

405 generally weaker potentials on the nightside than on the dayside and less sharp gradi-
 406 ents in the morphological variations. This is not to say that morphological dynamics on
 407 the nightside do not exist, but with respect to the phases of a geomagnetic storm, they
 408 are less clear than changes to the dayside. This does also not mean the nightside does
 409 not respond to dayside driving, but its responses are not ordered by storm phase. This
 410 is easily explained by the time-averaging that we have done: We know (see Table S1 in
 411 WG19) that the minimum and maximum durations of each storm phase can vary vastly
 412 (e.g. the recovery phase can be anything from ~ 6 to ~ 163 hours). By combining the data,
 413 such that the average convection maps match the median storm phases, we shift the data.
 414 Whilst the majority of storms are of similar length, it provides a good framework for study-
 415 ing the average storm-time responses, however other time-dependent phenomena, such
 416 as substorms are averaged out. It is well known that substorms occur frequently dur-
 417 ing geomagnetic storms and are important for the energisation of the ring current (e.g.
 418 Daglis, 2006; Sandhu et al., 2019), but Grocott et al. (2009) showed that substorms pri-
 419 marily produce a response in the high-latitude ionospheric convection pattern on the night-
 420 side and that ordering by onset location is important when trying to gain insight from
 421 the average convection pattern. It thus follows that although substorms commonly oc-
 422 cur during geomagnetic storms, averaging out over the substorm times and onset loca-
 423 tions means we do not see their signatures. We therefore cannot say if there is any or-
 424 dering by storm phase or time throughout the storm phases as no clear substorm sig-
 425 natures are seen in the average maps.

426 We see from Fig. 4 that the third component is primarily negative during the ini-
 427 tial phase, then increases to a positive value through the main phase and remains pri-
 428 marily positive throughout the recovery phase. This means that during the initial phase,
 429 \mathbf{X}_3^* is subtracted, and then during the main and recovery phases is added to the pattern.
 430 This will not only change the cross polar cap potential, increasing it during main and
 431 recovery phases and decreasing it during the initial phase, but it will also change the lo-
 432 cation of the dayside throat. In terms of the morphologies, this means the positive po-
 433 tential cell extends across the dayside towards the duskside at the beginning of the main
 434 phase. Then as the main phase progresses, the third eigenvector is added at increasing
 435 values, resulting in the negative cell extending over to magnetic noon and rotating the
 436 dayside convection throat to be more sun-aligned. Similarly, as the third eigenvector is
 437 added towards the end of the main phase, the fourth eigenvector, where the dayside po-

438 tential is the opposite, is subtracted which adds to this rotation. This may appear to be
 439 a result of solar wind driving and a change in the IMF B_Y component, which can move
 440 the dayside convection throat (e.g. Cowley & Lockwood, 1992; Thomas & Shepherd, 2018).
 441 This would be further evidenced as α_4^* shows a mild correlation (0.376) with the IMF
 442 B_Y component. We see however from the top panel in Fig. 4 that the average IMF B_Y
 443 component is near zero for these storms. In fact, 37% of the time the IMF B_Y compo-
 444 nent is positive for these storms, 38% of the time the IMF B_Y component is negative and
 445 it is zero the rest of the time. We see that it is the IMF B_Z component, which is enhanced
 446 during the main phase of the storm. That the average storm does thus not have a strong
 447 dusk-dawn component modulating the dayside flows (i.e. neither positive B_Y , nor neg-
 448 ative B_Y are consistently dominant) is also shown in Figure 2 (panel j) in WG19, which
 449 shows that during the main phase of the storm, the IMF is overwhelmingly southward
 450 for all storms considered here. Usually when SuperDARN maps are created, base-models,
 451 which are in part parameterised by the solar wind are used (e.g. Thomas & Shepherd,
 452 2018) such that datagaps are overcome. In this study however, no solar wind inputs were
 453 used at all as the data coverage is very good when combining data from 7 years of ge-
 454 omagnetic storms. We conclude that some of this rotation in the dayside throat may be
 455 due to an IMF B_Y component, but we speculate that there are other mechanisms at play
 456 due to the inconsistency in the directionality of the B_Y component.

457 We theorize that some of the control in the dayside throat rotating could due to
 458 a number of factors (or combination thereof): higher solar wind driving and the dayside
 459 reconnection rate increasing, or due to feedback through other means (e.g. thermospheric
 460 winds (Billett et al., 2018) and/or SEDs modulating the location of the throat (Zou et
 461 al., 2013, 2014) and/or the plasmaspheric plume impacting the magnetopause recon-
 462 necton rate post-noon). Further evidence for the plasmaspheric plume being responsible
 463 for this rotation of the dayside convection throat is available from comparing our results
 464 to those of Wharton et al. (2020): In their paper, Wharton et al. (2020) looked at the
 465 eigenfrequencies in ground magnetometer variations on the dayside during the same storm
 466 phases as ours. They found that that at L-shells < 4 , the eigenfrequencies in magnetome-
 467 ter measurements increase during the main phase of geomagnetic storms, which is due
 468 to the decrease in the plasma mass density caused by plasmaspheric erosion. This ap-
 469 proximately corresponds to a geomagnetic latitude of 60° or less (see table 1 in Wharton
 470 et al. (2020)), which corresponds to the dayside throat location we see during the main

471 phase of the storm. Wharton et al. (2020) find that at $L > 4$ (which maps to higher lat-
472 itudes and thus inside the convection pattern on the dayside), the eigenfrequencies de-
473 crease by $\sim 50\%$ during the main phase, due to a weaker magnetic field and an enhanced
474 plasma mass density. This may be further evidence of the plasmaspheric plume. Over-
475 all however, to find a conclusive answer for this rotation of the dayside throat further
476 studies are needed.

477 Gillies et al. (2011) studied line-of-sight SuperDARN velocity measurements dur-
478 ing geomagnetic storms and found that an increase in IMF B_Z is accompanied by a speed
479 increase measured with SuperDARN in the noon sector (9 to 15 MLT) and midnight sec-
480 tor (21 to 3 MLT) during the main phase. Gillies et al. (2011) also found a reduction
481 in the measured plasma drift early in the main phase for intense storms, and speculated
482 this either to be due to a reduction in the plasma drift speed or a change in the direc-
483 tion of the drift relative to the SuperDARN radar beam. In this study we have shown
484 (see Fig. 4), that the addition to the convection potential increases during this time (due
485 to the first, second and third components), which means that the convection potential
486 increases and thus ionospheric convection velocities are likely to be also increasing. This
487 is supported by our previous analysis (WG19) which showed that the cross polar cap po-
488 tential increases during this time and thus the convection should also increase. This pro-
489 vides further evidence that the decrease in the plasma drifts seen by Gillies et al. (2011)
490 during the main phase is due to the change in the direction of the flows relative to the
491 SuperDARN radar beam (i.e. the second of their two theories).

492 Cousins et al. (2015); Shi et al. (2020) used Empirical Orthogonal Function anal-
493 ysis to describe the modes of the Field Aligned Currents. Shi et al. (2020) split the data
494 according to different solar wind drivers, including High Speed Streams (HSS) and tran-
495 sient flows related to coronal mass ejections (CMEs), both of which can be drivers of ge-
496 omagnetic storms. Their patterns reflect the prevalence of the dual cell electrostatic pat-
497 tern that we also see, but due to different data binning, their modes are different, mak-
498 ing a direct comparison difficult. Overall, Shi et al. (2020) found that Sym-H is highly
499 correlated with the modes in the transient flow category, indicating that strong geomag-
500 netic storm activity dominates this category, which gives a strong dual cell convection
501 pattern, as well as expansions and contractions. Both their HSS and transient categories
502 show a mode which gives a strong asymmetry on the dayside (and would result in a sim-
503 ilar rotation to the dayside throat that we see), which are highly correlated with Sym-

504 H activity, but also the IMF B_Y and B_X components, and AE and solar wind temper-
 505 ature. Whilst the data presented by Cousins et al. (2015) did not contain any consid-
 506 erable geomagnetic storm activity, their results generally agree with the results from Shi
 507 et al. (2020). What does stand out when comparing results however, is that their first
 508 mode shows, similar to Shi et al. (2020) a strengthening of the pattern, which is highly
 509 correlated with AE and the IMF B_Z component. This is followed by a mode describing
 510 the expansions and contractions, which is correlated with B_Y , AE and Sym-H. The third
 511 mode from Cousins et al. (2015), describes the cusp shaping, which is also correlated with
 512 B_Y , AE and tilt, but not Sym-H. It is worth noting that as Cousins et al. (2015) only
 513 showed the first few modes, and their chosen time period contains little geomagnetic ac-
 514 tivity. Cousins et al. (2013) on the other hand, used the EOF analysis to study Super-
 515 DARN data. They analysed 20 months of plasma drift data to study electric field vari-
 516 ability and found that the first component accounted for $\sim 50\%$ of the observed total squared
 517 electric field (which is as a proxy for the electrostatic energy per unit volume) and is pri-
 518 marily responsible for variations on long timescales (~ 1 hr). It is worth noting that their
 519 components look different to ours as they used a different dataset (i.e. their K_p median
 520 was 1, so they used a non-storm time dataset) for input but in general find the two-cell
 521 convection pattern to be dominant as well. Comparison between our data, Shi et al. (2020),
 522 Cousins et al. (2013) and Cousins et al. (2015) shows that using different data brings out
 523 different modes with different properties: the primary EOF in Cousins et al. (2015) strength-
 524 ens the convection pattern, whereas the secondary component has a shaping function,
 525 followed by expanding and rotating modes. They further find that their top correlation
 526 for the first component is at 0.44 for the AE index, which is considerably lower than our
 527 top correlation (0.808) coefficient between Sym-H and the first component. The dayside
 528 throat in the patterns (mean and components) shown by Cousins et al. (2013) show no
 529 rotation: their mean is perfectly aligned with noon, which we attribute to the fact that
 530 their input data is on average from both positive and negative B_Y with no storm effects.
 531 Conversely, the mean pattern from Milan (2015), where they applied the principal com-
 532 ponent analysis to a much larger dataset of the Birkeland currents inferred by AMPERE,
 533 showed a rotation in the throat which aligns with 11 and 23 MLT. This is comparable
 534 to the average conditions, also when studying SuperDARN data (e.g. Thomas & Shep-
 535 herd, 2018) and indicates that the mean and the components are susceptible to the in-
 536 put data.

537 As part of this study we have provided a first analysis of how the dayside throat
 538 responds to geomagnetic storms (i.e. internal magnetospheric dynamics), versus IMF B_Y
 539 conditions (i.e. external magnetospheric dynamics) and studied the timescales of day-
 540 side throat changes with respect to geomagnetic storms. In order to understand this fully,
 541 requires further study. If the dayside throat is rotated due to the plasmaspheric plume
 542 mechanism, we would expect to see the same rotation (away from dusk) in the south-
 543 ern hemisphere, but we would expect to see a rotation in the opposite sense in the south-
 544 ern hemisphere for any IMF B_Y related effect. We have provided a first order analysis
 545 of this and discussed potential mechanisms here but in order to find a more definitive
 546 answer, southern hemisphere data will be investigated in more detail in a future study.

547 6 Summary

548 We have utilised SuperDARN line-of-sight ionospheric plasma measurements to study
 549 ionospheric electric potential morphologies during geomagnetic storm time and specif-
 550 ically geomagnetic storm phases. We applied a principal component analysis to average
 551 ionospheric convection maps to examine the primary morphological features for the first
 552 time and using eigenvalue decomposition, we see how dominant patterns change over time
 553 (i.e. through the storm phases). The main dynamics in the morphologies that we have
 554 uncovered are happening to the ionospheric electric potential pattern on a large scale:
 555 the electric potential pattern expands and contracts; the potentials increase and decrease
 556 in strength; and the dayside convection throat rotates. We speculate that all these changes
 557 are due to the IMF B_Z component of the solar wind increasing during the main phase
 558 of the storm.

559 We find that

- 560 1. the first 6 eigenvectors describe over $\sim 90\%$ of variance.
- 561 2. the two-cell convection pattern is dominant as is expected due to an expected high
 562 level of solar wind driving.
- 563 3. the first eigenvector, \mathbf{X}_1^* , provides an increase or decrease in two-cell convection
 564 strength and is highly correlated with Sym-H ($|r|=0.803$).
- 565 4. \mathbf{X}_2^* provides a way to increase/decrease the dusk/dawn cells and thus add asym-
 566 metry (but no clear change is seen by storm phase).

- 567 5. \mathbf{X}_3^* provides a strengthening of the dual-cell convection pattern and a rotation of
 568 the dayside convection throat.
- 569 6. \mathbf{X}_4^* to \mathbf{X}_6^* provide further ways of adding asymmetry and changes to the dual-cell
 570 convection pattern, primarily on the dayside.
- 571 7. most of the average morphological changes are on the dayside.
- 572 8. the electric potential increases through the main phase and then decreases as soon
 573 as the recovery phase is reached.
- 574 9. the dayside convection throat points towards afternoon sector before the main phase
 575 and then as the electric potential increases, the dayside throat rotates towards noon.

576 Acknowledgments

577 All data used for this study are available opensource from nonprofit organizations. The
 578 authors acknowledge the use of SuperDARN data. SuperDARN is a collection of radars
 579 funded by national scientific funding agencies of Australia, Canada, China, France, Japan,
 580 South Africa, United Kingdom, and United States of America, and we thank the inter-
 581 national PI team for providing the data. The authors acknowledge access to the Super-
 582 DARN database via the Virginia Tech SuperDARN group and their website (<http://vt.superdarn.org/>).
 583 Other data mirrors are hosted by the British Antarctic Survey (<https://www.bas.ac.uk/project/superdarn/#data>)
 584 and the University of Saskatchewan (<https://superdarn.ca/data-download>). The Radar
 585 Software Toolkit (RST) to process the SuperDARN data can be downloaded from Zen-
 586 odo (<https://doi.org/10.5281/zenodo.1403226> and references). The combined data which
 587 are used to plot the maps and are used to perform the principal component analysis are
 588 available from the Lancaster University's research archive (PURE), DOI:10.17635/lancaster/researchdata/344.
 589 M.-T. W. and A. G. were supported by Natural Environments Research Council (NERC),
 590 UK, grant nos. NE/P001556/1 and NE/T000937/1. S.E.M. was supported by the Sci-
 591 ence and Technology Facilities Council (STFC), UK, grant no. ST/S000429/1.

592 References

- 593 Akasofu, S.-I., & Chapman, S. (1961). The ring current, geomagnetic disturbance,
 594 and the van allen radiation belts. *Journal of Geophysical Research (1896-*
 595 *1977)*, *66*(5), 1321-1350. doi: 10.1029/JZ066i005p01321
- 596 Baker, J. B., Ridley, A. J., Papitashvili, V. O., & Clauer, C. R. (2003). The
 597 dependence of winter aurora on interplanetary parameters. *Journal of*

- 598 *Geophysical Research: Space Physics*, 108(A4). Retrieved from [https://](https://agupubs.onlinelibrary.wiley.com/doi/abs/10.1029/2002JA009352)
599 agupubs.onlinelibrary.wiley.com/doi/abs/10.1029/2002JA009352 doi:
600 10.1029/2002JA009352
- 601 Billett, D. D., Grocott, A., Wild, J. A., Walach, M.-T., & Kosch, M. J. (2018).
602 Diurnal variations in global joule heating morphology and magnitude due to
603 neutral winds. *Journal of Geophysical Research: Space Physics*, 123(3), 2398-
604 2411. Retrieved from [https://agupubs.onlinelibrary.wiley.com/doi/abs/](https://agupubs.onlinelibrary.wiley.com/doi/abs/10.1002/2017JA025141)
605 [10.1002/2017JA025141](https://agupubs.onlinelibrary.wiley.com/doi/abs/10.1002/2017JA025141) doi: 10.1002/2017JA025141
- 606 Chapman, S., & Bartels, J. (1940). *Geomagnetism, Vol. II: Analysis of the Data and*
607 *Physical Theories*. Oxford University Press.
- 608 Chapman, S., & Dyson, F. W. (1918). An outline of a theory of magnetic storms.
609 *Proceedings of the Royal Society of London. Series A, Containing Papers*
610 *of a Mathematical and Physical Character*, 95(666), 61-83. Retrieved from
611 <https://royalsocietypublishing.org/doi/abs/10.1098/rspa.1918.0049>
612 doi: 10.1098/rspa.1918.0049
- 613 Chapman, S., & Ferraro, V. C. A. (1930). A new theory of magnetic storms. *Nature*,
614 126(3169), 129–130. doi: 10.1038/126129a0
- 615 Chisham, G., Lester, M., Milan, S. E., Freeman, M. P., Bristow, W. a., Grocott, a.,
616 ... Walker, a. D. M. (2007). A decade of the Super Dual Auroral Radar Net-
617 work (SuperDARN): Scientific achievements, new techniques and future direc-
618 tions. *Surveys in Geophysics*, 28(1), 33–109. doi: 10.1007/s10712-007-9017-8
- 619 Cousins, E. D. P., Matsuo, T., & Richmond, A. D. (2013). Mesoscale and large-
620 scale variability in high-latitude ionospheric convection: Dominant modes and
621 spatial/temporal coherence. *Journal of Geophysical Research: Space Physics*,
622 118(12), 7895-7904. Retrieved from [https://agupubs.onlinelibrary.wiley](https://agupubs.onlinelibrary.wiley.com/doi/abs/10.1002/2013JA019319)
623 [.com/doi/abs/10.1002/2013JA019319](https://agupubs.onlinelibrary.wiley.com/doi/abs/10.1002/2013JA019319) doi: 10.1002/2013JA019319
- 624 Cousins, E. D. P., Matsuo, T., Richmond, A. D., & Anderson, B. J. (2015). Dom-
625 inant modes of variability in large-scale birkeland currents. *Journal of Geo-*
626 *physical Research: Space Physics*, 120(8), 6722-6735. Retrieved from [https://](https://agupubs.onlinelibrary.wiley.com/doi/abs/10.1002/2014JA020462)
627 agupubs.onlinelibrary.wiley.com/doi/abs/10.1002/2014JA020462 doi:
628 10.1002/2014JA020462
- 629 Cowley, S. W. H., & Lockwood, M. (1992). Excitation and decay of solar wind-
630 driven flows in the magnetosphere-ionosphere system. *Annales geophys-*

- 631 *icae*, 10, 103–115. Retrieved from [http://cat.inist.fr/?aModele=](http://cat.inist.fr/?aModele=afficheN{\&}cpsidt=5295768)
632 [afficheN{\&}cpsidt=5295768](http://cat.inist.fr/?aModele=afficheN{\&}cpsidt=5295768)
- 633 Daglis, I. A. (2006, Jun 01). Ring current dynamics. *Space Science Reviews*, 124(1),
634 183–202. Retrieved from <https://doi.org/10.1007/s11214-006-9104-z>
635 doi: 10.1007/s11214-006-9104-z
- 636 Daglis, I. A., Thorne, R. M., Baumjohann, W., & Orsini, S. (1999). The terrestrial
637 ring current: Origin, formation, and decay. *Reviews of Geophysics*, 37(4), 407-
638 438. doi: 10.1029/1999RG900009
- 639 Dungey, J. W. (1961, Jan). Interplanetary magnetic field and the auroral zones.
640 *Phys. Rev. Lett.*, 6, 47–48. Retrieved from [https://link.aps.org/doi/](https://link.aps.org/doi/10.1103/PhysRevLett.6.47)
641 [10.1103/PhysRevLett.6.47](https://link.aps.org/doi/10.1103/PhysRevLett.6.47) doi: 10.1103/PhysRevLett.6.47
- 642 Dungey, J. W. (1963). Interactions of solar plasma with the geomagnetic
643 field. *Planetary and Space Science*, 10, 233 - 237. Retrieved from
644 <http://www.sciencedirect.com/science/article/pii/0032063363900205>
645 doi: [https://doi.org/10.1016/0032-0633\(63\)90020-5](https://doi.org/10.1016/0032-0633(63)90020-5)
- 646 Foster, J. C. (1993). Storm time plasma transport at middle and high latitudes.
647 *Journal of Geophysical Research: Space Physics*, 98(A2), 1675-1689. Retrieved
648 from [https://agupubs.onlinelibrary.wiley.com/doi/abs/10.1029/](https://agupubs.onlinelibrary.wiley.com/doi/abs/10.1029/92JA02032)
649 [92JA02032](https://agupubs.onlinelibrary.wiley.com/doi/abs/10.1029/92JA02032) doi: 10.1029/92JA02032
- 650 Gabrielse, C., Pinto, V., Nishimura, Y., Lyons, L., Gallardo-Lacourt, B., & Deng, Y.
651 (2019). Storm time mesoscale plasma flows in the nightside high-latitude iono-
652 sphere: A statistical survey of characteristics. *Geophysical Research Letters*,
653 46(8), 4079-4088. Retrieved from [https://agupubs.onlinelibrary.wiley](https://agupubs.onlinelibrary.wiley.com/doi/abs/10.1029/2018GL081539)
654 [.com/doi/abs/10.1029/2018GL081539](https://agupubs.onlinelibrary.wiley.com/doi/abs/10.1029/2018GL081539) doi: 10.1029/2018GL081539
- 655 Gillies, D. M., McWilliams, K. A., St. Maurice, J.-P., & Milan, S. E. (2011). Global-
656 scale observations of ionospheric convection during geomagnetic storms.
657 *Journal of Geophysical Research: Space Physics*, 116(A12). Retrieved
658 from [https://agupubs.onlinelibrary.wiley.com/doi/abs/10.1029/](https://agupubs.onlinelibrary.wiley.com/doi/abs/10.1029/2011JA017086)
659 [2011JA017086](https://agupubs.onlinelibrary.wiley.com/doi/abs/10.1029/2011JA017086) doi: 10.1029/2011JA017086
- 660 Gillies, D. M., St.-Maurice, J.-P., McWilliams, K. A., & Milan, S. (2012).
661 Global-scale observations of ionospheric convection variation in response
662 to sudden increases in the solar wind dynamic pressure. *Journal of Geo-*
663 *physical Research: Space Physics*, 117(A4). Retrieved from <https://>

- 664 agupubs.onlinelibrary.wiley.com/doi/abs/10.1029/2011JA017255 doi:
665 10.1029/2011JA017255
- 666 Gonzalez, W. D., Joselyn, J. A., Kamide, Y., Kroehl, H. W., Rostoker, G., Tsuru-
667 tani, B. T., & Vasyliunas, V. M. (1994, April). What is a geomagnetic storm?
668 *Journal of Geophysical Research*, *99*, 5771-5792. doi: 10.1029/93JA02867
- 669 Graham, G. (1724). Iv. an account of observations made of the variation of the
670 horizontal needle at london, in the latter part of the year 1772, and beginning
671 of 1723. *Philosophical Transactions of the Royal Society of London*, *33*(383),
672 96-107. doi: 10.1098/rstl.1724.0020
- 673 Greenwald, R. A., Baker, K. B., Dudeney, J. R., Pinnock, M., Jones, T. B., Thomas,
674 E. C., ... Yamagishi, H. (1995). Darn/superdarn. *Space Science Reviews*,
675 *71*(1), 761-796. doi: 10.1007/BF00751350
- 676 Grocott, A., Milan, S. E., Imber, S. M., Lester, M., & Yeoman, T. K. (2012). A
677 quantitative deconstruction of the morphology of high-latitude ionospheric con-
678 vection. *Journal of Geophysical Research: Space Physics*, *117*(A5). Retrieved
679 from [https://agupubs.onlinelibrary.wiley.com/doi/abs/10.1029/
680 2012JA017580](https://agupubs.onlinelibrary.wiley.com/doi/abs/10.1029/2012JA017580) doi: 10.1029/2012JA017580
- 681 Grocott, A., Wild, J. A., Milan, S. E., & Yeoman, T. K. (2009). Super-
682 posed epoch analysis of the ionospheric convection evolution during sub-
683 storms: onset latitude dependence. *Annales Geophysicae*, *27*(2), 591-
684 600. Retrieved from <https://www.ann-geophys.net/27/591/2009/> doi:
685 10.5194/angeo-27-591-2009
- 686 Hairston, M. R., & Heelis, R. A. (1993). *High-latitude electric field studies using*
687 *dmsp data* (Tech. Rep.). Texas University at Dallas Richardson Center for
688 Space Sciences.
- 689 Heppner, J. P., & Maynard, N. C. (1987). Empirical high-latitude electric field
690 models. *Journal of Geophysical Research*, *92*(A5), 4467-4489. doi: 10.1029/
691 JA092iA05p04467
- 692 Huba, J. D., Joyce, G., Sazykin, S., Wolf, R., & Spiro, R. (2005). Simulation
693 study of penetration electric field effects on the low- to mid-latitude iono-
694 sphere. *Geophysical Research Letters*, *32*(23). Retrieved from [https://
695 agupubs.onlinelibrary.wiley.com/doi/abs/10.1029/2005GL024162](https://agupubs.onlinelibrary.wiley.com/doi/abs/10.1029/2005GL024162) doi:
696 10.1029/2005GL024162

- 697 Hutchinson, J. A., Wright, D. M., & Milan, S. E. (2011). Geomagnetic storms over
698 the last solar cycle: A superposed epoch analysis. *Journal of Geophysical Re-*
699 *search: Space Physics*, *116*(9), 1–16. doi: 10.1029/2011JA016463
- 700 Imber, S. M., Milan, S. E., & Lester, M. (2013). The heppner-maynard bound-
701 ary measured by superdarn as a proxy for the latitude of the auroral oval.
702 *Journal of Geophysical Research: Space Physics*, *118*(2), 685-697. doi:
703 10.1029/2012JA018222
- 704 Iyemori, T. (1990). Storm-time magnetospheric currents inferred from mid-latitude
705 geomagnetic field variations. *Journal of geomagnetism and geoelectricity*,
706 *42*(11), 1249-1265. doi: 10.5636/jgg.42.1249
- 707 Joliffe, I. T. (2002). *Principle component analysis*. Springer.
- 708 Kamide, Y., Richmond, A. D., & Matsushita, S. (1981). Estimation of ionospheric
709 electric fields, ionospheric currents, and field-aligned currents from ground
710 magnetic records. *Journal of Geophysical Research: Space Physics*, *86*(A2),
711 801-813. Retrieved from [https://agupubs.onlinelibrary.wiley.com/doi/](https://agupubs.onlinelibrary.wiley.com/doi/abs/10.1029/JA086iA02p00801)
712 [abs/10.1029/JA086iA02p00801](https://agupubs.onlinelibrary.wiley.com/doi/abs/10.1029/JA086iA02p00801) doi: 10.1029/JA086iA02p00801
- 713 Kane, T. A., & Makarevich, R. A. (2010). Hf radar observations of the f region
714 ionospheric plasma response to storm sudden commencements. *Journal of Geo-*
715 *physical Research: Space Physics*, *115*(A7). Retrieved from [https://agupubs](https://agupubs.onlinelibrary.wiley.com/doi/abs/10.1029/2009JA014974)
716 [.onlinelibrary.wiley.com/doi/abs/10.1029/2009JA014974](https://agupubs.onlinelibrary.wiley.com/doi/abs/10.1029/2009JA014974) doi: 10.1029/
717 2009JA014974
- 718 Kikuchi, T., Hashimoto, K. K., & Nozaki, K. (2008). Penetration of magneto-
719 spheric electric fields to the equator during a geomagnetic storm. *Journal*
720 *of Geophysical Research: Space Physics*, *113*(A6). Retrieved from [https://](https://agupubs.onlinelibrary.wiley.com/doi/abs/10.1029/2007JA012628)
721 agupubs.onlinelibrary.wiley.com/doi/abs/10.1029/2007JA012628 doi:
722 10.1029/2007JA012628
- 723 Kim, H.-J., Lyons, L. R., Ruohoniemi, J. M., Frissell, N. A., & Baker, J. B. (2012).
724 Principal component analysis of polar cap convection. *Geophysical Research*
725 *Letters*, *39*(11). Retrieved from [https://agupubs.onlinelibrary.wiley](https://agupubs.onlinelibrary.wiley.com/doi/abs/10.1029/2012GL052083)
726 [.com/doi/abs/10.1029/2012GL052083](https://agupubs.onlinelibrary.wiley.com/doi/abs/10.1029/2012GL052083) doi: 10.1029/2012GL052083
- 727 Lin, C. H., Richmond, A. D., Heelis, R. A., Bailey, G. J., Lu, G., Liu, J. Y., ...
728 Su, S.-Y. (2005). Theoretical study of the low- and midlatitude iono-
729 spheric electron density enhancement during the october 2003 superstorm:

- 730 Relative importance of the neutral wind and the electric field. *Journal of*
 731 *Geophysical Research: Space Physics*, 110(A12). Retrieved from [https://](https://agupubs.onlinelibrary.wiley.com/doi/abs/10.1029/2005JA011304)
 732 agupubs.onlinelibrary.wiley.com/doi/abs/10.1029/2005JA011304 doi:
 733 10.1029/2005JA011304
- 734 Loewe, C. A., & Prölss, G. W. (1997). Classification and mean behavior of mag-
 735 netic storms. *Journal of Geophysical Research: Space Physics*, 102(A7), 14209-
 736 14213. doi: 10.1029/96JA04020
- 737 Mannucci, A. J., Tsurutani, B. T., Abdu, M. A., Gonzalez, W. D., Komjathy, A.,
 738 Echer, E., ... Anderson, D. (2008). Superposed epoch analysis of the day-
 739 side ionospheric response to four intense geomagnetic storms. *Journal of*
 740 *Geophysical Research: Space Physics*, 113(A3). Retrieved from [https://](https://agupubs.onlinelibrary.wiley.com/doi/abs/10.1029/2007JA012732)
 741 agupubs.onlinelibrary.wiley.com/doi/abs/10.1029/2007JA012732 doi:
 742 10.1029/2007JA012732
- 743 Milan, S. E. (2015). Magnetospheric Plasma Physics: The Impact of Jim Dungey's
 744 Research. In D. Southwood, S. W. H. Cowley FRS, & S. Mitton (Eds.), *Mag-*
 745 *netospheric plasma physics: The impact of jim dungey's research* (pp. 1–271).
 746 doi: 10.1007/978-3-319-18359-6_2
- 747 Milan, S. E., Carter, J. A., Korth, H., & Anderson, B. J. (2015). Principal com-
 748 ponent analysis of birkeland currents determined by the active magnetosphere
 749 and planetary electrodynamics response experiment. *Journal of Geophysical*
 750 *Research: Space Physics*, 120(12), 10,415-10,424. Retrieved from [https://](https://agupubs.onlinelibrary.wiley.com/doi/abs/10.1002/2015JA021680)
 751 agupubs.onlinelibrary.wiley.com/doi/abs/10.1002/2015JA021680 doi:
 752 10.1002/2015JA021680
- 753 Milan, S. E., Clausen, L. B. N., Coxon, J. C., Carter, J. A., Walach, M.-T., Laundal,
 754 K., ... Anderson, B. J. (2017). Overview of solar wind–magnetosphere–
 755 ionosphere–atmosphere coupling and the generation of magnetospheric cur-
 756 rents. *Space Science Reviews*, 206(1), 547–573. Retrieved from [https://](https://doi.org/10.1007/s11214-017-0333-0)
 757 doi.org/10.1007/s11214-017-0333-0 doi: 10.1007/s11214-017-0333-0
- 758 Milan, S. E., Gosling, J. S., & Hubert, B. (2012, mar). Relationship between inter-
 759 planetary parameters and the magnetopause reconnection rate quantified from
 760 observations of the expanding polar cap. *Journal of Geophysical Research*,
 761 117(A3), A03226. doi: 10.1029/2011JA017082
- 762 Nishitani, N., Ruohoniemi, J. M., Lester, M., Baker, J. B. H., Koustov, A. V., Shep-

- 763 herd, S. G., ... Kikuchi, T. (2019). Review of the accomplishments of mid-
 764 latitude super dual auroral radar network (superdarn) hf radars. *Progress in*
 765 *Earth and Planetary Science*, 6(1), 27. doi: 10.1186/s40645-019-0270-5
- 766 Press, W. H., Teukolsky, S. A., T., V. W., & P., F. B. (2007). *Numerical recipes:*
 767 *The art of scientific computing*. Cambridge University Press.
- 768 Ruohoniemi, J. M., & Baker, K. B. (1998). Large-scale imaging of high-latitude con-
 769 vection with Super Dual Auroral Radar Network HF radar observations. *Jour-*
 770 *nal of Geophysical Research*, 103(A9), 20797. doi: 10.1029/98JA01288
- 771 Ruohoniemi, J. M., & Greenwald, R. A. (1996). Statistical patterns of high-latitude
 772 convection obtained from Goose Bay HF radar observations. *Journal of Geo-*
 773 *physical Research*, 101(A10), 21743. Retrieved from [http://doi.wiley.com/](http://doi.wiley.com/10.1029/96JA01584)
 774 [10.1029/96JA01584](http://doi.wiley.com/10.1029/96JA01584) doi: 10.1029/96JA01584
- 775 Sandhu, J. K., Rae, I. J., Freeman, M. P., Gkioulidou, M., Forsyth, C., Reeves,
 776 G. D., ... Walach, M.-T. (2019). Substorm-ring current coupling: A
 777 comparison of isolated and compound substorms. *Journal of Geophysi-*
 778 *cal Research: Space Physics*, 124(8), 6776-6791. Retrieved from [https://](https://agupubs.onlinelibrary.wiley.com/doi/abs/10.1029/2019JA026766)
 779 agupubs.onlinelibrary.wiley.com/doi/abs/10.1029/2019JA026766 doi:
 780 [10.1029/2019JA026766](https://agupubs.onlinelibrary.wiley.com/doi/abs/10.1029/2019JA026766)
- 781 Shepherd, S. G., & Ruohoniemi, J. M. (2000). Electrostatic potential patterns in
 782 the high-latitude ionosphere constrained by superdarn measurements. *Journal*
 783 *of Geophysical Research: Space Physics*, 105(A10), 23005-23014. Retrieved
 784 from [https://agupubs.onlinelibrary.wiley.com/doi/abs/10.1029/](https://agupubs.onlinelibrary.wiley.com/doi/abs/10.1029/2000JA000171)
 785 [2000JA000171](https://agupubs.onlinelibrary.wiley.com/doi/abs/10.1029/2000JA000171) doi: 10.1029/2000JA000171
- 786 Shi, Y., Knipp, D. J., Matsuo, T., Kilcommons, L., & Anderson, B. (2020). Modes
 787 of (facs) variability and their hemispheric asymmetry revealed by inverse and
 788 assimilative analysis of iridium magnetometer data. *Journal of Geophysical Re-*
 789 *search: Space Physics*, 125(2), e2019JA027265. Retrieved from [https://](https://agupubs.onlinelibrary.wiley.com/doi/abs/10.1029/2019JA027265)
 790 agupubs.onlinelibrary.wiley.com/doi/abs/10.1029/2019JA027265
 791 [\(e2019JA027265 2019JA027265\)](https://agupubs.onlinelibrary.wiley.com/doi/abs/10.1029/2019JA027265) doi: 10.1029/2019JA027265
- 792 Shore, R. M., Freeman, M. P., & Gjerloev, J. W. (2018). An empirical orthogonal
 793 function reanalysis of the northern polar external and induced magnetic field
 794 during solar cycle 23. *Journal of Geophysical Research: Space Physics*, 123(1),
 795 781-795. Retrieved from [https://agupubs.onlinelibrary.wiley.com/doi/](https://agupubs.onlinelibrary.wiley.com/doi/abs/10.1029/2018JA025600)

- 796 abs/10.1002/2017JA024420 doi: 10.1002/2017JA024420
- 797 Singer, S. F. (1957). A new model of magnetic storms and aurorae. *Eos,*
798 *Transactions American Geophysical Union, 38(2)*, 175-190. doi: 10.1029/
799 TR038i002p00175
- 800 Siscoe, G. L., & Huang, T. S. (1985). Polar cap inflation and deflation. *Journal of*
801 *Geophysical Research, 90(A1)*, 543–547.
- 802 Sugiura, M. (1964). Hourly values of equatorial dst for the igy. *Ann. Int. Geophys.*
803 *Yr., 35*, 9.
- 804 SuperDARN Data Analysis Working Group, P. m., Thomas, E. G., Ponomarenko,
805 P. V., Billett, D. D., Bland, E. C., Burrell, A. G., ... Walach, M.-T. (2018,
806 August). *Superdarn radar software toolkit (rst) 4.2*. Retrieved from
807 <https://doi.org/10.5281/zenodo.1403226> doi: 10.5281/zenodo.1403226
- 808 Thomas, E. G., Baker, J. B. H., Ruohoniemi, J. M., Clausen, L. B. N., Coster, A. J.,
809 Foster, J. C., & Erickson, P. J. (2013). Direct observations of the role of
810 convection electric field in the formation of a polar tongue of ionization from
811 storm enhanced density. *Journal of Geophysical Research: Space Physics,*
812 *118(3)*, 1180-1189. Retrieved from [https://agupubs.onlinelibrary.wiley](https://agupubs.onlinelibrary.wiley.com/doi/abs/10.1002/jgra.50116)
813 [.com/doi/abs/10.1002/jgra.50116](https://agupubs.onlinelibrary.wiley.com/doi/abs/10.1002/jgra.50116) doi: 10.1002/jgra.50116
- 814 Thomas, E. G., & Shepherd, S. G. (2018, apr). Statistical Patterns of Ionospheric
815 Convection Derived From Mid-latitude, High-Latitude, and Polar Super-
816 DARN HF Radar Observations. *Journal of Geophysical Research: Space*
817 *Physics, 123(4)*, 3196–3216. Retrieved from [http://doi.wiley.com/10.1002/](http://doi.wiley.com/10.1002/2018JA025280)
818 2018JA025280 doi: 10.1002/2018JA025280
- 819 Walach, M.-T. (2020). *Ionospheric electric field morphologies during geo-*
820 *magnetic storm phases*. Lancaster University PURE. Retrieved from
821 <https://dx.doi.org/10.17635/lancaster/researchdata/344> doi:
822 10.17635/lancaster/researchdata/344
- 823 Walach, M.-T., & Grocott, A. (2019). Superdarn observations during geomagnetic
824 storms, geomagnetically active times, and enhanced solar wind driving. *Jour-*
825 *nal of Geophysical Research: Space Physics, 124(7)*, 5828-5847. Retrieved
826 from [https://agupubs.onlinelibrary.wiley.com/doi/abs/10.1029/](https://agupubs.onlinelibrary.wiley.com/doi/abs/10.1029/2019JA026816)
827 2019JA026816 doi: 10.1029/2019JA026816
- 828 Walach, M.-T., Milan, S. E., Yeoman, T. K., Hubert, B. A., & Hairston, M. R.

- 829 (2017). Testing nowcasts of the ionospheric convection from the expand-
830 ing and contracting polar cap model. *Space Weather*, 15(4), 623-636. doi:
831 10.1002/2017SW001615
- 832 Wharton, S. J., Rae, I. J., Sandhu, J. K., Walach, M.-T., Wright, D. M., & Yeoman,
833 T. K. (2020). The changing eigenfrequency continuum during geomagnetic
834 storms: Implications for plasma mass dynamics and ulf wave coupling. *Journal*
835 *of Geophysical Research: Space Physics*, n/a(n/a), e2019JA027648. Retrieved
836 from [https://agupubs.onlinelibrary.wiley.com/doi/abs/10.1029/](https://agupubs.onlinelibrary.wiley.com/doi/abs/10.1029/2019JA027648)
837 [2019JA027648](https://agupubs.onlinelibrary.wiley.com/doi/abs/10.1029/2019JA027648) (e2019JA027648 2019JA027648) doi: 10.1029/2019JA027648
- 838 Wilson, G. R., Burke, W. J., Maynard, N. C., Huang, C. Y., & Singer, H. J. (2001).
839 Global electrodynamics observed during the initial and main phases of the
840 july 1991 magnetic storm. *Journal of Geophysical Research: Space Physics*,
841 106(A11), 24517-24539. doi: 10.1029/2000JA000348
- 842 Zou, S., Moldwin, M. B., Ridley, A. J., Nicolls, M. J., Coster, A. J., Thomas, E. G.,
843 & Ruohoniemi, J. M. (2014). On the generation/decay of the storm-enhanced
844 density plumes: Role of the convection flow and field-aligned ion flow. *Jour-*
845 *nal of Geophysical Research: Space Physics*, 119(10), 8543-8559. Retrieved
846 from [https://agupubs.onlinelibrary.wiley.com/doi/abs/10.1002/](https://agupubs.onlinelibrary.wiley.com/doi/abs/10.1002/2014JA020408)
847 [2014JA020408](https://agupubs.onlinelibrary.wiley.com/doi/abs/10.1002/2014JA020408) doi: 10.1002/2014JA020408
- 848 Zou, S., Ridley, A. J., Moldwin, M. B., Nicolls, M. J., Coster, A. J., Thomas, E. G.,
849 & Ruohoniemi, J. M. (2013). Multi-instrument observations of sed during
850 2425 october 2011 storm: Implications for sed formation processes. *Jour-*
851 *nal of Geophysical Research: Space Physics*, 118(12), 7798-7809. Retrieved
852 from [https://agupubs.onlinelibrary.wiley.com/doi/abs/10.1002/](https://agupubs.onlinelibrary.wiley.com/doi/abs/10.1002/2013JA018860)
853 [2013JA018860](https://agupubs.onlinelibrary.wiley.com/doi/abs/10.1002/2013JA018860) doi: 10.1002/2013JA018860

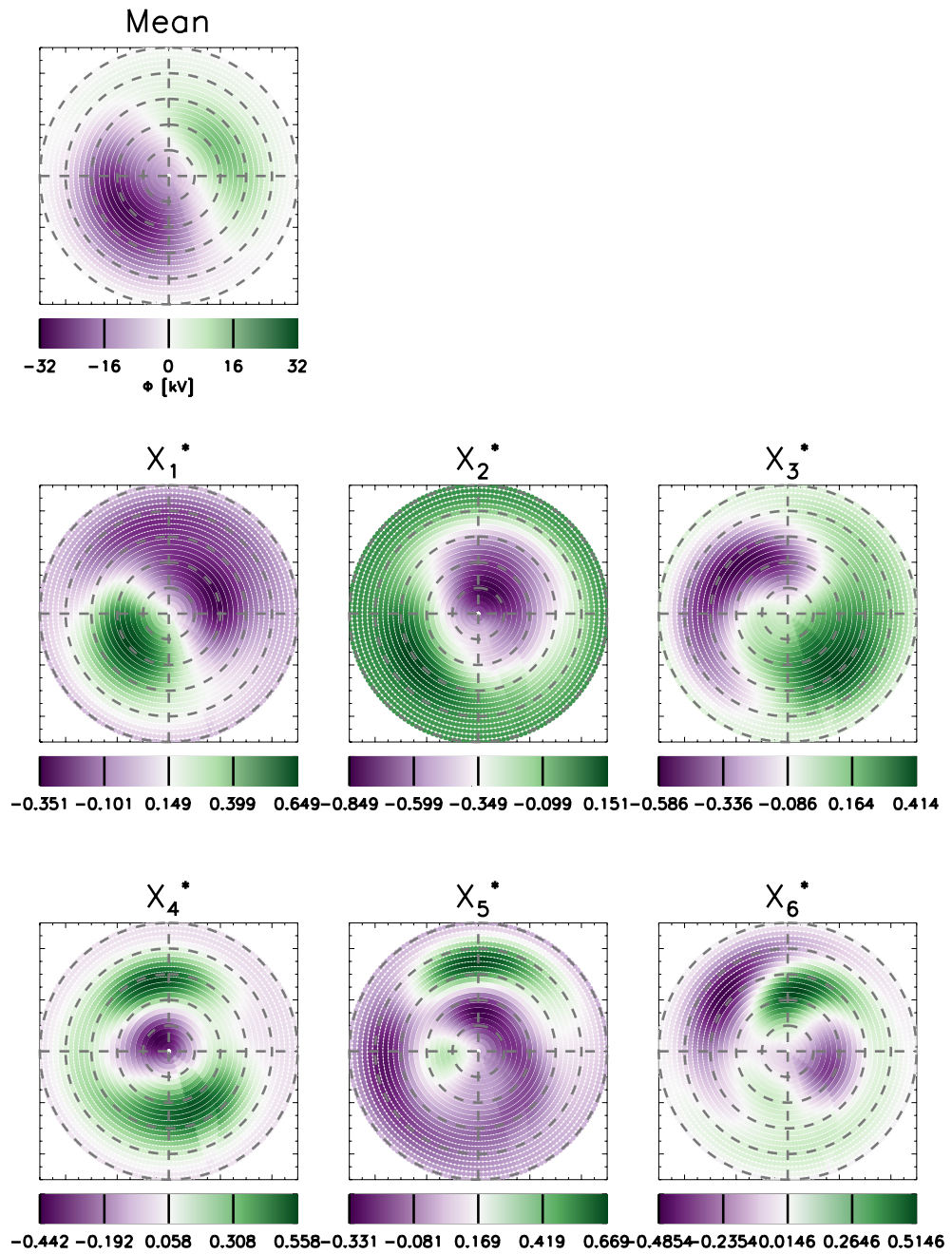


Figure 3. Ionospheric electric field component patterns showing the mean for geomagnetic storms (top left), followed by the patterns corresponding to the first 6 eigenvectors of the Principal Component Analysis, which have been normalised. Each pattern is centred on the geomagnetic pole, with 1200 magnetic local time pointing towards the top of the page, and dusk towards the left. Lines of geomagnetic latitudes are indicated from 40° to 90° by the dashed grey circles.

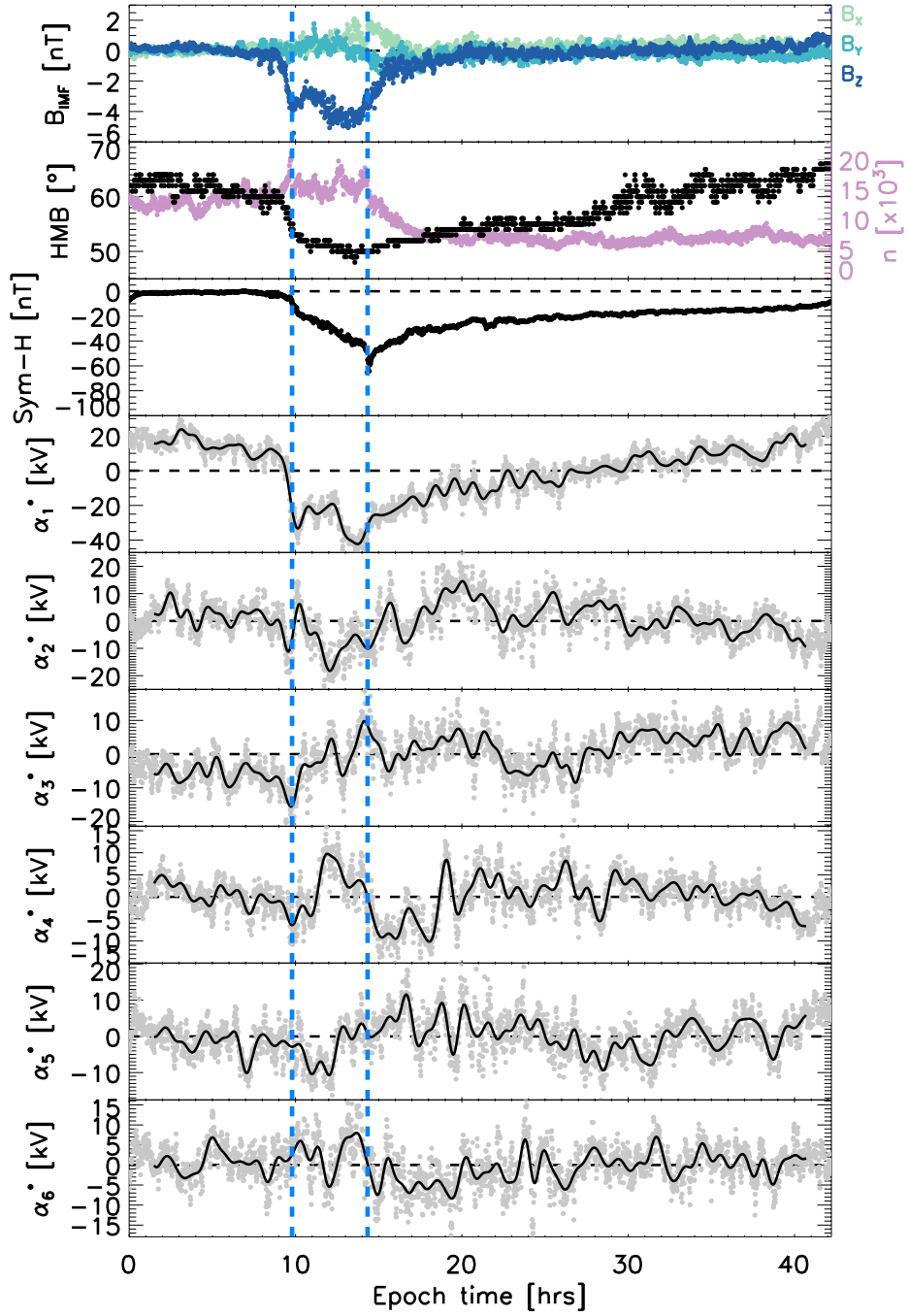


Figure 4. Panels showing the average (median) interplanetary magnetic field, B_{IMF} (top panel), where the light green is B_X , turquoise is B_Y and the dark blue is B_Z ; the Heppner Maynard Boundary and the number of backscatter points per average SuperDARN map (in rose) (second panel from the top); followed by the median Sym-H index and the first 6 normalised components of the Principal Component Analysis with respect to time through the storm phases. The components are shown in grey and the black lines shows them with a 60-minute low pass filter applied. The boundaries between the initial and main, and the main and recovery phases are shown by the dashed blue vertical lines. The third panel also shows the median Sym-H index in blue.